Nam, J.; Lee, J.; Park, H.; Park, C.; Lee, C.; Chung, J.; Lee, S.-G.; Kang, N.:

Alleviation of Hydrogen Embrittlement to Delay Effective Hydrogen Diffusion Against MA Constituent Formation Due to Mo Solutes for 420 MPa Grade Offshore Steels.

In: Metals and Materials International. Vol. 29 (2023) 1625-1636.

First published online by Springer: 19.11.2022

https://dx.doi.org/10.1007/s12540-022-01336-z

Alleviation of Hydrogen Embrittlement to Delay Effective Hydrogen Diffusion Against MA Constituent Formation Due to Mo Solutes for 420 MPa Grade Offshore Steels

Jimin Nam[1] · Junghoon Lee[2] · Hanji Park[3,4] · Cheolho Park[5] · Changhoon Lee[6] · Junho Chung[7] · Seung-gun Lee[6] · Namhyun Kang[1]

Abstract

Hydrogen embrittlement (HE) is a significant issue in high-strength offshore steel. Mo is added for high strength, and several studies on the HE resistance by Mo solutes and Mo segregation have been reported. However, the effect of Mo addition on HE in bainitic steels has not been studied yet. This study investigated the effect of increasing Mo content (up to 0.2 wt%) on HE resistance in terms of crack initiation and hydrogen diffusion behaviors in bainitic steels. With the addition of Mo, the strength of 0.2 Mo steel increased, but it's HE resistance was nearly identical to that of 0.02 Mo steel. As the Mo content increased, the martensite-austenite (MA) constituents sensitive to HE increased; however, the Mo solutes, which serve as trap sites for hydrogen, also increased. The delay in hydrogen diffusion by the Mo solutes played a role in alleviating the degradation in the HE resistance of the MA constituents of 0.2 Mo steel.

1 Introduction

The rapid increase in energy demand has led to the depletion of energy resources on land and in nearby marine areas. Fur-thermore, soaring oil prices and the low efficiency of renew-able energy are attracting attention toward polar regions and the deep sea as potential energy mining areas. This has resulted in an increase in steel demand for building offshore plant facilities. Offshore steels used in mega structures are mainly manufactured using a thermo-mechanical control process (TMCP). The high strength of offshore steel is required for size and safety issues; therefore, TMCP steel using bainitic microstructures has recently been developed [1, 2, 3, 4].

Various methods have been considered to produce steel with high strength, among which the addition of alloy ele-ments such as Ti, Nb, Cr, Mo, and V is the most commonly used one [5]. In particular, Mo is an alloying element that enhances hardenability, increases strength through solid solution hardening, precipitation hardening, and the solute drag effect [6, 7, 8], and facilitates the formation of bainite by delaying pearlite transformation. However, the high strength of steel often weakens its resistance to hydrogen embrittlement (HE) [9]. HE resistance is an important factor because offshore steels have been normally used in seawa-ter environments. Many studies have reported the effects of alloying elements on HE resistance. Zhang et al. [10] indi-cated that the addition of Nb to hot stamping steel with high strength improved the delayed fracturing resistance owing to the hydrogen trapping effect of NbC nanoparticles. Kim et al. [11] showed that the addition of Ti to hot-stamped boron steel reduced the prior austenite grain size and increased the amount of titanium carbide at the nanoscale,

✉ Namhyun Kang
nhkang@pusan.ac.kr

[1] Pusan National University, Busan 46241, Republic of Korea

[2] Helmholtz-Zentrum Hereon, Max-Planck-Str. 1, 21502 Geesthacht, Germany

[3] Portland State University, Portland, OR 97201, USA

[4] Inha University, Incheon 22212, Republic of Korea

[5] Chosun University, Gwangju 61452, Republic of Korea

[6] Korea Institute of Materials Science, Changwon 51508, Republic of Korea

[7] Hyundai Steel Company, Chungnam 31719, Republic of Korea

serving as an irreversible hydrogen trap site, and providing relatively good HE resistance. Yoo et al. [6] reported that Mo solutes reduced hydrogen and strain localization on prior austenite grain boundary, and the grain boundary cohesion increased owing to Mo segregation, thereby decreasing the reduction in the elongation caused by hydrogen. While most studies have investigated martensitic steel, bainitic steel has a far more complex microstructure than martensitic steel. Bainitic steel comprises various constituents such as acicular ferrite (AF), degenerated pearlite (DP), bainite, and martensite-austenite (MA), which exhibit different hydrogen-diffusion behaviors [12], and the degree of HE varies depending on the microstructure fraction [13].

The present study evaluated the HE resistance of bainitic steels with varying Mo contents produced using the TMCP process. The changes in the microstructure, HE mechanism, and hydrogen diffusion behavior based on the Mo content were analyzed, and the relationship between them was investigated. Thus, this study investigates the effect of Mo solutes on the HE resistance of offshore steel.

2 Experimental

2.1 Materials and Microstructural Analysis

The chemical composition of the steels used in this study is listed in Table 1. To investigate the effect of Mo, these steels were designed with Mo contents of 0.02 and 0.2 wt%. Two specimens were prepared in a vacuum induction melting furnace. The 30 kg ingots with 100 mm thickness were hot-rolled to plates with 12 mm thickness. The ingots were soaked at 1200 °C for 2 h, followed by hot rolling at a temperature higher than 950 °C and air-cooling. The specimens were mechanically polished and chemically etched using nitric acid solution (2 vol%). The microstructures were observed using light optical microscopy (LOM) and field emission scanning electron microscopy (FESEM). The MA constituent fraction was averaged by analyzing 10 LOM images (500 magnification) etched by LePera etchant using image analysis software. To investigate the grain size and strain distribution, electron backscattered diffraction (EBSD) was performed at an acceleration voltage of 15 kV, working distance of 20 mm, and step size of 0.15 µm. Field-emission transmission electron microscopy (FETEM, TalosF200X) was performed to identify the microstructure. The FETEM specimens were prepared using a focused ion beam (FIB) to determine the MA constituents, and a replica method was used to observe the type and size of the precipitates.

2.2 In-Situ Slow Strain Rate Testing (SSRT)

The mechanical properties were analyzed using SSRT under two conditions: in-air (without hydrogen charging) and H (with hydrogen charging). The SSRT specimens were extracted in the rolling direction at a 1/4t thickness of the steel and fabricated without notches according to the sub-size standard of ASTM E8 with a gauge length of 25 mm, gauge width of 6 mm, and thickness of 3 mm. The specimens were polished to 2000 grit using SiC paper, and the SSRT was performed at a nominal strain rate of 10^{-5}/s, where hydrogen diffusion was considered during tensile testing. To saturate the specimen with hydrogen, the sample was electrochemically pre-charged at a current density of 5 A/m^2 for 24 h using a 3% NaCl + 0.3% NH_4SCN aqueous solution, and the same condition was also applied during SSRT [14]. SSRT fractography of the in-air and H environments was analyzed using FESEM to measure the cross-sectional reduction area.

2.3 Hydrogen Permeation Test

Hydrogen permeation tests were performed on a thin steel membrane according to the ISO17081 standard test method to observe hydrogen diffusion behavior. The steel membrane was sampled parallel to the rolling direction at a 1/4t thickness of the steel. Both sides of the steel membrane were mechanically ground to 2000 grit using SiC paper, and the final thickness of the steel membranes was 480 (± 15) µm. The detection side of the steel membrane was coated with Pd to prevent surface corrosion. Pd coating was applied using an ion sputter coater with a current of 5 mA for 300 s. The exposed area of the steel membrane located between the detection and charging cell was 78.5 mm^2. Hydrogen was absorbed on the charging side at a constant current density of 5 A/m^2 using a 3% NaCl + 0.3% NH_4SCN solution. The detection side was maintained at a constant voltage of + 250 mV relative to the 3 M KCl-Ag/AgCl electrode using a 0.1 M NaOH solution. The oxygen in the solution of

Table 1 Chemical composition of 420 MPa-grade steels used in the study (wt%)

Specimens	C	Si	Mn	Cu	Cr	Ni	Mo	Nb	Ti	Al	N, ppm
0.02 Mo	0.09	0.22	1.5	0.15	0.085	0.07	0.02	0.05	0.015	0.02	5
0.2 Mo	0.09	0.22	1.5	0.15	0.085	0.1	0.2	0.05	0.015	0.02	5

the detection and charging cell was removed by continuously injecting nitrogen gas.

2.4 Silver Decoration and Thermal Desorption Spectroscopy (TDS)

Silver decoration and TDS were performed to analyze the hydrogen-trapping behavior. The specimen used for silver decoration was made of a disk with a diameter of 25 mm and thickness of 1 mm. The specimens were mechanically polished to 1 μm and chemically etched using 2 vol% nitric acid solution. The etched specimens were charged with a mixed aqueous solution of 3% NaCl and 0.3% NH_4SCN at a current density of $5A/m^2$ for 2 h. After saturating the specimen with hydrogen, the applied current was turned off, and the specimen was left in the solution for a certain period of time (5 min and 1 h). The specimens were then immersed in an aqueous 2.15 mM $KAg(CN)_2$ solution for 1 3 h and washed with distilled water. The dimensions of the specimens used in TDS were $55 \times 10 \times 3$ mm. The specimens were polished with SiC paper and hydrogen-charged under the same conditions as the in situ SSRT. TDS was performed at a heating rate of 200 ℃/h.

3 Results

3.1 Microstructure with Respect to the Content of Mo

Figure 1 shows the microstructures observed by LOM and FESEM with respect to the Mo content. In 0.02 Mo steel, polygonal ferrite (PF) was the main microstructure with degenerated pearlite (DP) and martensite-austenite (MA) constituents (Fig. 1a and c). The 0.2 Mo steel was dominated by granular bainite (GB) with a lath subgrain boundary within the ferrite and secondary phases, cementite, and MA constituents (Fig. 1b and d). The GB was more dominant in 0.2 Mo steel than in 0.02 Mo steel. Table 2 summarizes the grain sizes (d_G) of each steel measured using EBSD. The grain size decreased from 17 to 11 μm as the Mo content increased from 0.02 to 0.2 wt%.

Figure 2 shows the amount of MA constituents etched in a LePera solution in which ferrite appeared yellow or blue, bainite appeared brown, and MA constituents appeared white [15]. A very small amount of MA constituents was observed among the DPs in the 0.02 Mo steel, whereas large amounts of irregular MA constituents were observed in the entire area of the 0.2 Mo steel. The quantified fraction of MA constituents is shown in Table 2. 0.2 Mo steel exhibited 1.39 vol% that was larger than that of the 0.02 Mo steel (0.05 vol%). In other words, the bainite and MA constituent fractions increased with the Mo content. This was in agreement with the previous results [2, 16], where Mo increases the activation energy of C diffusion, and slower rate of carbon diffusion during the accelerated cooling process delays the reaction between ferrite and pearlite.

Figure 3 shows FETEM micrographs of the replica specimens to investigate the effect of Mo on the precipitates. Both 0.02 Mo and 0.2 Mo steels showed (Ti,Nb)C and CuS precipitates (Fig. 3a). Figure 3b and c show the distribution and amount of precipitates in both specimens. The 0.02 Mo and 0.2 Mo steels exhibit similar distributions and amounts of precipitates. Mo precipitates from the surface of pre-existing precipitates through aging and inhibits the growth of existing precipitates [7]. Owing to the lack of aging for precipitation, the precipitate behavior did not change with Mo content, and most Mo solutes in the 0.2 Mo steel were mostly dissolved in the matrix [6]. Therefore, the effect of the precipitate based on the Mo contents was excluded from the HE behavior, which has been explained in the discussion section.

3.2 In-Situ SSRT Properties and Crack Behavior with Respect to Hydrogen Charging and Mo Addition

Figure 4 shows the engineering tensile stress-strain curves for the specimens in various environments: in air and H. For the in-air condition, the yield-point phenomenon owing to discontinuous yielding behavior was observed for 0.02Mo steel (black line in Fig. 4a), whereas this phenomenon was not observed for 0.2Mo steel (black line in Fig. 4b). The yield-point phenomenon was caused by the interaction between interstitial solute atoms and dislocations during tensile testing. The carbon diffusion into dislocations to produce a dislocation pair was suppressed because Mo increases the activation energy of the carbon diffusion [17]. Thus, the yield point phenomenon was not observed when 0.2 wt%. Mo was added. Furthermore, 0.2 Mo steel under in-air conditions has a higher yield strength (YS) and tensile strength (TS) than 0.02 Mo steel. Table 3 lists the quantitative values of each tensile curve for varying Mo contents. The YS and TS of 0.2 Mo steel and hardenability increased, while the elongation decreased owing to solid solution strengthening, grain refinement, and bainite formation [7, 16, 18].

Regardless of the Mo content, the H condition produced a YS and TS similar to that of the in-air condition, but both steels showed a significant decrease in elongation under the H condition (red lines in Fig. 4a and b). Fig. 5 shows the fracture surfaces of each specimen after the SSRT. The in-air specimens exhibited necking and a large cross-sectional reduction (Fig. 5a and e), which was associated with a large elongation (black lines in Fig. 4). However, the H specimens showed no necking and very little cross-sectional reduction (Fig. 5c), correlating with rapidly decreasing elongation after hydrogen charging (red

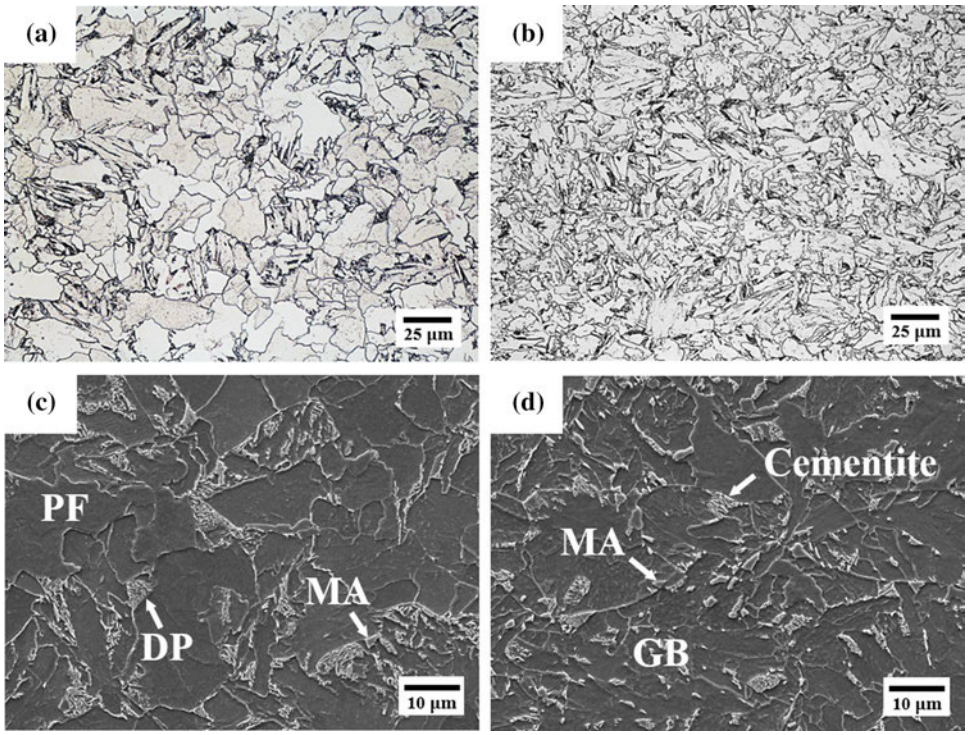

Fig. 1 Microstructures measured by LOM **a**, **b** and FESEM **c**, **d** for varying Mo contents: **a**, **c** 0.02 Mo, **b**, **d** 0.2 Mo

Table 2 Grain size (d_G) and MA constituent fraction of 0.02 Mo and 0.2 Mo steels

	0.02 Mo	0.2 Mo
d_G (μm)	17 (±1.6)	11 (±0.6)
MA constituents fraction (%)	0.05 (±0.03)	1.39 (±0.36)

lines in Fig. 4). The detailed fracture surface showed that the in-air specimens had ductile dimple fractures (Fig. 5b and f), whereas the H specimens had brittle quasi-cleavage fractures (Fig. 5d and h). The cross-sectional reduction rates of 0.02 Mo and 0.2 Mo steels were measured from Fig. 5a, c, e, and g, which showed significant variations for in-air condition (75.6 and 73.6%, respectively) and H conditions (29.0 and 21.3%, respectively). The drastic drop in the elongation or cross-sectional area under in-air and H conditions is a typical feature of HE, which is mechanically degraded by hydrogen [19, 20]. To compare the hydrogen embrittlement resistance with Mo addition, the hydrogen embrittlement index (HE index) was calculated using the following equation [21, 22]:

$$\text{HE index}(\%) = \left| \frac{\varepsilon_{in-air} - \varepsilon_H}{\varepsilon_{in-air}} \right| \times 100 \quad (1)$$

where $\varepsilon_{\text{in-air}}$ and ε_H represent the elongations under the in-air and H conditions, respectively. The HE index obtained using Eq. 1 is summarized in Table 3. The HE index of both steels were almost the same (46.1 and 49.3%). Despite the bainite

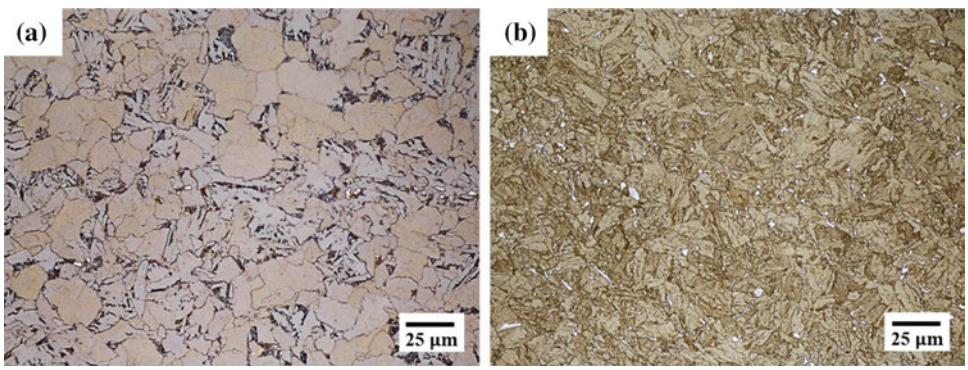

Fig. 2 Optical micrographs of microstructures etched in LePera solution for varying Mo contents: **a** 0.02 Mo, **b** 0.2 Mo

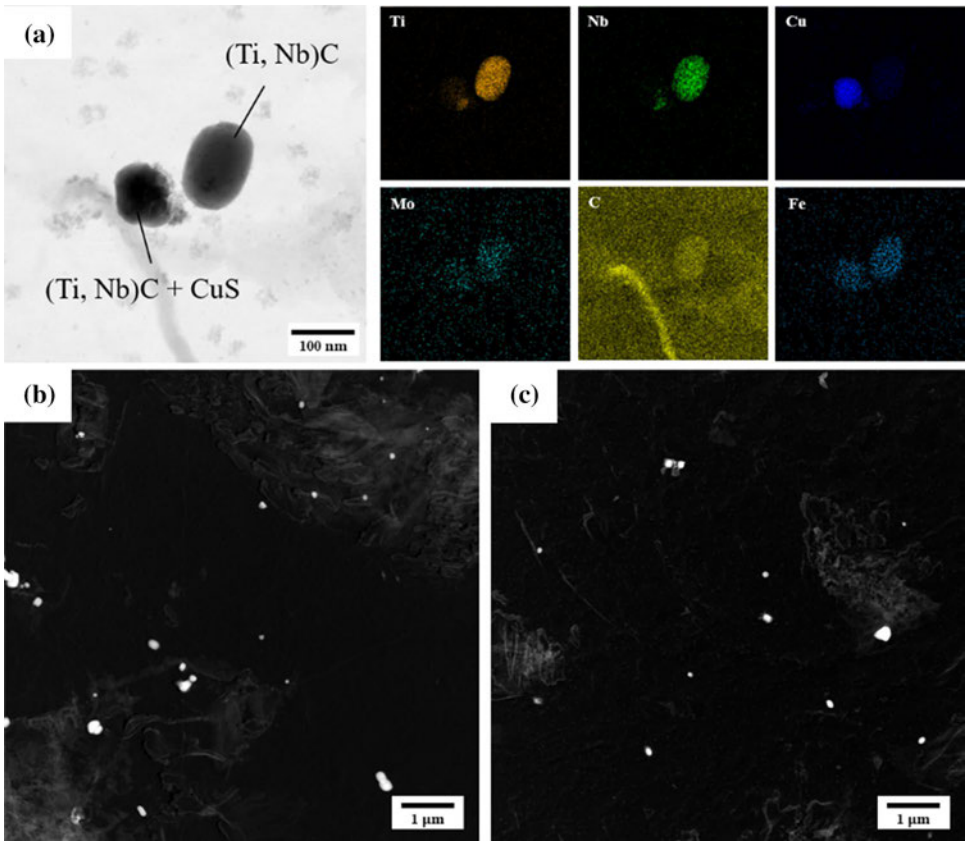

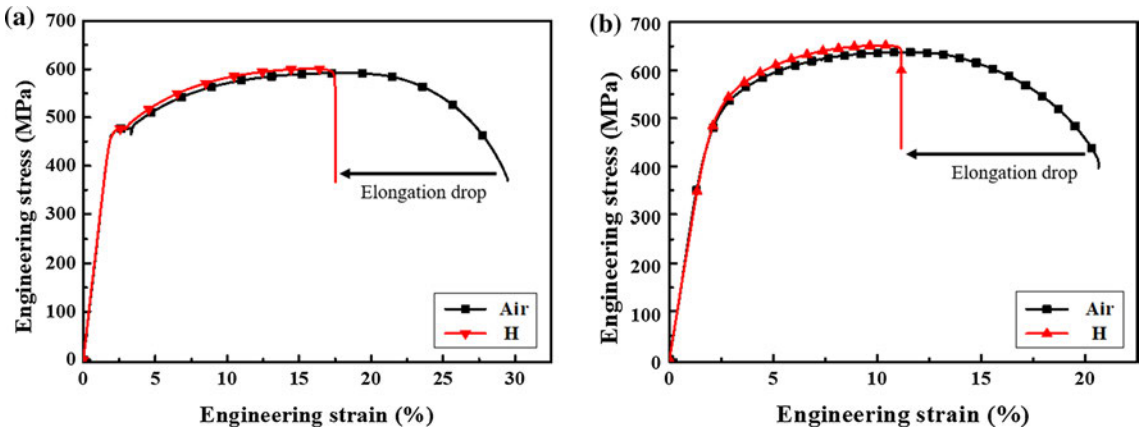

Fig. 3 FETEM micrographs: **a** Bright-field image and EDS mapping for 0.2 Mo steel, **b**, **c** dark-field images of precipitates for 0.02 Mo and 0.2 Mo steels, respectively

Fig. 4 Engineering stress–strain curves conducted by SSRT for varying conditions (in-air and H) and Mo contents: **a** 0.02 Mo, **b** 0.2 Mo

structure formation and changes in YS (~15 MPa) and TS (~43 MPa) owing to 0.2 wt% Mo addition, both steels exhibited similar HE resistance.

To investigate the effect of microstructural variations on crack initiation in the HE environment, cross-sections of the fractured specimens after SSRT were observed, as shown in Fig. 6. The microstructure of 0.02 and 0.2 Mo steels for the in-air condition showed elongated morphology along the loading direction (Fig. 6a and e). Numerous cracks/voids were observed at the interface between the secondary phases and ferrite and in the broken cementite inside the DP (Fig. 6b and f).

In contrast, the H condition showed that the microstructure hardly stretched after the SSRT (Fig. 6c and g), and secondary cracks that occurred perpendicular to the loading direction were observed (Fig. 6d and h). These results can explain the elongation drop and brittle fracture that appeared during the in situ SSRT with hydrogen charging.

Table 3 SSRT properties at various environments (in-air and H)

Specimens	Conditions	YS (MPa)	TS (MPa)	El (%)	HE index (%)
0.02 Mo steel	In-air	457 (±4.19)	600 (±5.91)	29.3 (±0.12)	46.1
	H	460 (±5.91)	609 (±6.24)	15.8 (±1.36)	
0.2 Mo steel	In-air	470 (±7.32)	644 (±7.32)	20.7 (±0.54)	49.3
	H	477 (±5.25)	652 (±1.63)	10.5 (±0.53)	

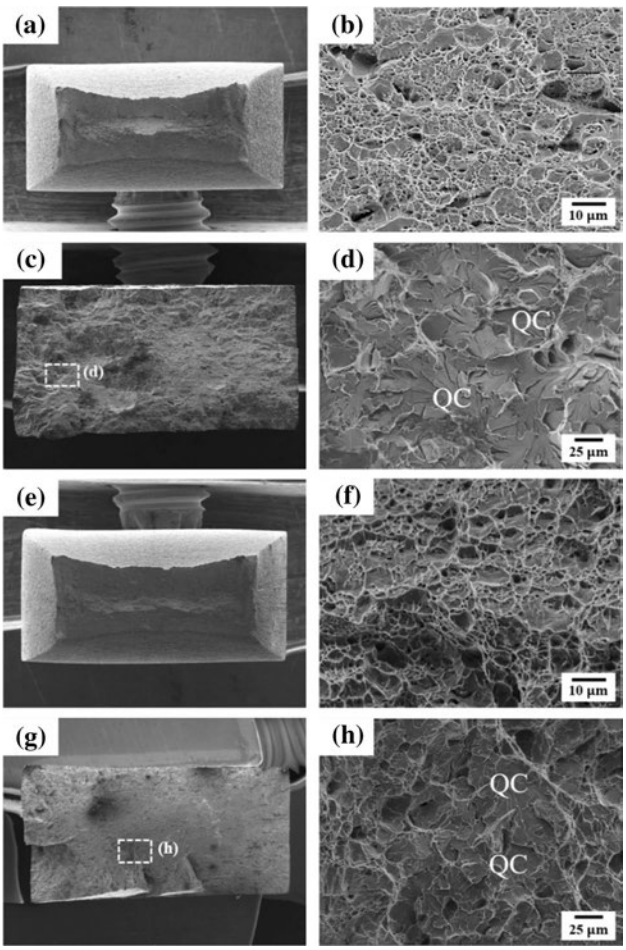

Fig. 5 Fracture surface of in-air **a**, **b**, **e**, **f** and H **c**, **d**, **g**, **h** specimens for various Mo contents: **a**–**d** 0.02 Mo, **e**–**h** 0.2 Mo

In particular, secondary cracks in 0.02 Mo steel (Fig. 6d) and 0.2 Mo steel (Fig. 6h) occurred at various positions with various morphologies under H conditions. In Fig. 6, the yellow arrows indicate MA constituents. The 0.2 Mo steel had more MA constituents (yellow arrows in Fig. 6h) than the 0.02 Mo steel (yellow arrows in Fig. 6d). White arrows (cracks or voids) in the 0.02 Mo steel were not specifically related to yellow arrows (MA constituents) and were observed at various locations, such as the interface between MA constituents and DP, matrix, grain boundary, and within grains (Fig. 6d). However, most of the white arrows (cracks) in the 0.2 Mo steel were located with yellow arrows (MA constituents), and secondary cracks occurred at the interface of the MA constituents or in the MA constituents (Fig. 6h). Fig. 7 shows the EBSD results of the secondary crack periphery of H-charged specimen after SSRT. The area indicated by the yellow line represents cracks. Figs. 7a and b show the IQ and KAM maps, respectively, for 0.02 Mo steel. The IQ map of 0.02 Mo steel shows very small secondary cracks, and a heavily deformed DP compared to ferrite. The KAM map can be used to observe the strain distribution through misorientation, and the degree of deformation and KAM value increased simultaneously as the color varies from blue to red 1, [23]. In the KAM map for 0.02 Mo steel, the DP periphery appeared green, indicating a large deformation. Most structures of the 0.2 Mo steel were uniformly deformed in the IQ map (Fig. 7c), and secondary cracks across the MA constituents, indicated by red arrows, were observed. Relatively large deformations were observed near the MA constituents in the KAM map (Fig. 7d). Park et al. [24] reported that very small cracks in pearlite and blunt crack tips propagated along the loading direction by stretching the ferrite matrix, and crack propagation along the loading direction was associated with a high HE resistance. However, MA constituents are stress-concentrated sites and are prone to crack initiation. Therefore, the HE resistance of 0.2 Mo steel containing numerous MA constituents should be low because of the sharp crack tip [14, 25]. However, the 0.02 and 0.2 Mo steels exhibited the same HE index; therefore, further discussion is needed in the coming section.

4 Discussion

Figure 8 shows the TDS results for the hydrogen-charged steels in association with the SSRT results. The reversible hydrogen desorption curve of 0.2 Mo steel at ~ 110 °C was higher than that of the 0.02 Mo steel. Furthermore, the amount of hydrogen measured below 400 °C was 0.25 and 0.63 wppm, respectively, for 0.02 and 0.2 Mo steels. This indicates that during SSRT, 0.2 Mo steel has more reversible hydrogen than 0.02 Mo steel [26]. However, regardless of the Mo content, very low desorption curves were observed at 425 500 °C. Low desorption curves at high

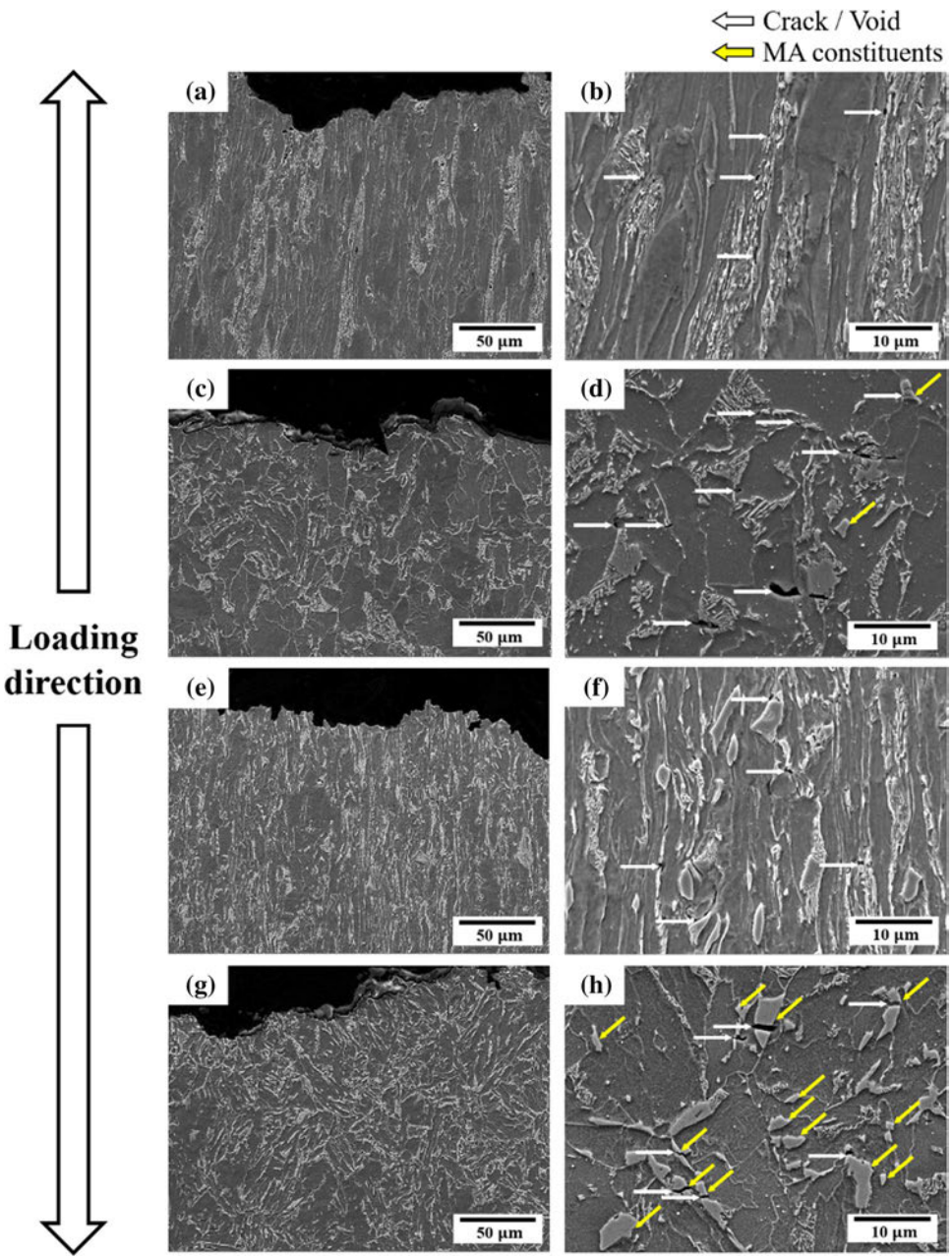

Fig. 6 SEM micrographs of the secondary cracks and voids in the cross section of various specimens: **a**, **b**, **e**, **f** in-air, **c**, **d**, **g**, **h** H, **a**–**d** 0.02 Mo, **e**–**h** 0.2 Mo

temperature were associated with very small levels of irreversible hydrogen.

Therefore, the diffusion and trap behaviors of reversible hydrogen in each steel were compared through a permeation test. The 1st permeation was performed to saturate the reversible and irreversible trap sites with hydrogen, thereby releasing reversible hydrogen, and leaving irreversible hydrogen in the specimen. The 2nd permeation was conducted to measure the permeation result of reversible hydrogen only, and the results are shown in Fig. 9. The permeation graph shows the results from the entry of electrochemically generated hydrogen into the specimen to the steady state of saturated hydrogen inside the specimen [27–29]. The graph of 0.2 Mo steel has a lower slope compared to that of 0.02 Mo steel, indicating that it takes longer to obtain the same current density using 0.2 Mo steel. In other words, the 0.2 Mo steel showed a slower diffusion rate than the 0.02 Mo steel.

The permeation result was used to calculate the effective diffusion coefficient (D_{eff}) and reversible hydrogen trap density (C_{rev}) using the following equations [30–32], and the results are shown in Table 4.

$$D_{eff}\left(\frac{m^2}{s}\right) = \frac{L^2}{6t_{lag}} \quad (2)$$

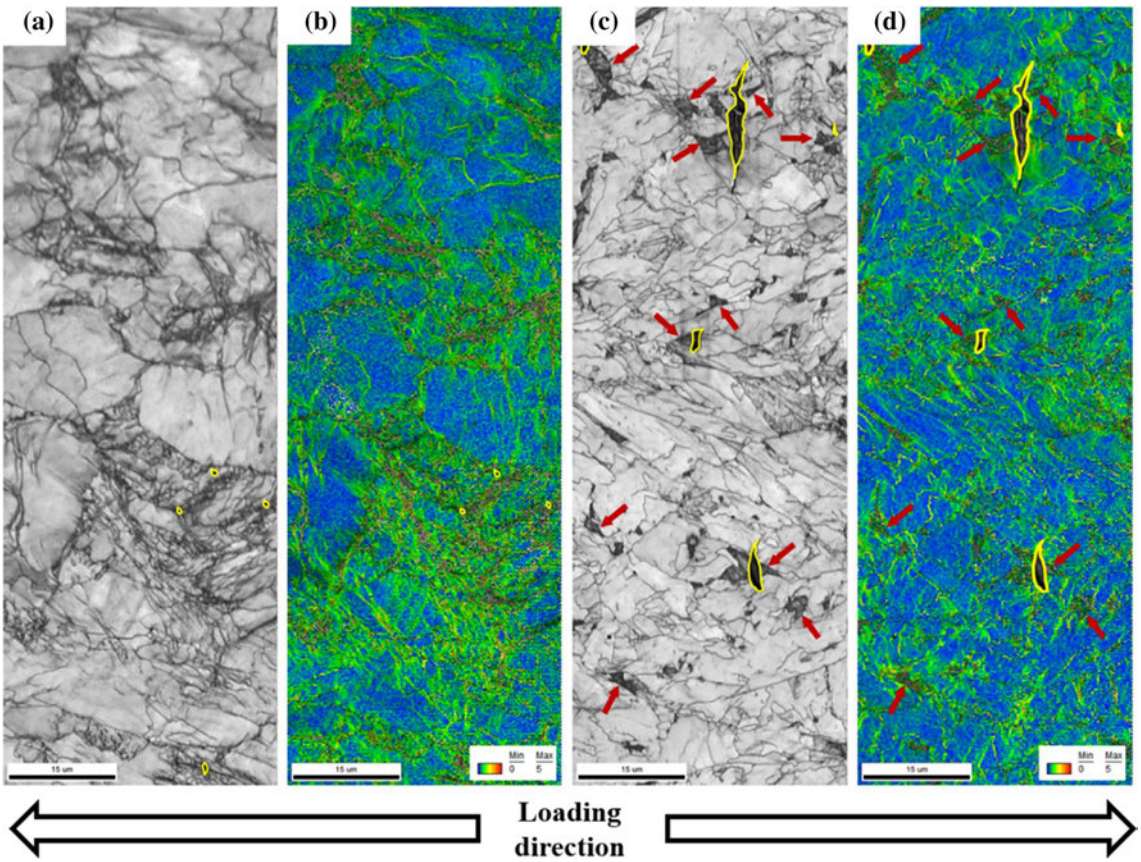

Fig. 7 EBSD maps of **a**, **c** image quality and **b**, **d** KAM after in situ SSRT for various specimens: **a**, **b** 0.02 Mo, **c**, **d** 0.2 Mo

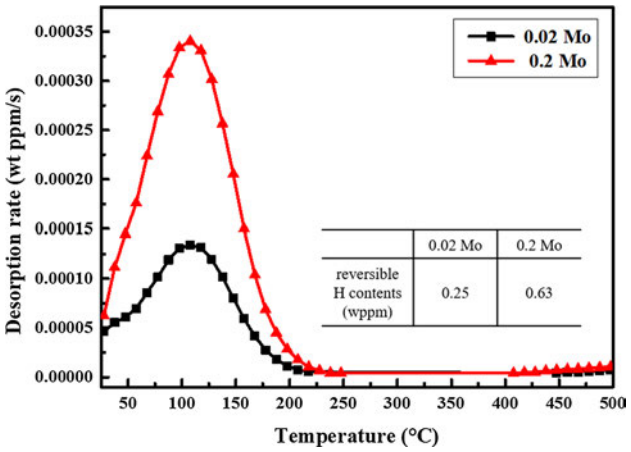

Fig. 8 Reversible and irreversible hydrogen desorbed from 0.02 Mo and 0.2 Mo specimens

$$C_{rev}\left(\frac{mol}{m^3}\right) = \frac{J_{SS}L}{D_{eff}} = \frac{I_{SS}L}{D_{eff}F} \tag{3}$$

where L is the thickness of the specimen, t_{lag} is the time at which $J(t)/J_{SS}$ is 0.63, J_{SS} is the hydrogen flow rate in the steady state, I_{SS} is the current density in the steady state, and F is Faraday's constant (F=96,485 C/mol). In Fig. 9, the D_{eff} of 0.2 Mo steel with a low slope of the permeation curve, was 1.49×10^{-10} m^2/s, and a smaller apparent diffusion coefficient was observed compared to the D_{eff} (2.39×10^{-10} m^2/s) for 0.02 Mo steel. It was necessary to examine the relationship between the microstructure and diffusion rate because the diffusion rate affects the initiation and propagation of cracks. Furthermore, the variation in microstructures has a significant effect on HE because the microstructures that affect the diffusion rate serve as trap sites for hydrogen [13, 33]. In particular, the C_{rev} of 0.2 Mo steel was 0.77 mol/m^3, which was 1.7 times larger than 0.45 mol/m^3 of 0.02 Mo steel, and showed the same tendency as that of the TDS result (Fig. 6) [34]. It is judged that the apparent diffusion coefficient of 0.2 Mo steel was low because 0.2 Mo steel had a larger fraction of microstructure, serving as a trap site for reversible hydrogen, such as a large area of grain boundary induced by a small grain size and heavily deformed microstructures (GB and MA).

Figure 10 shows the micrographs of the microstructure serving as a trap site for reversible hydrogen through silver

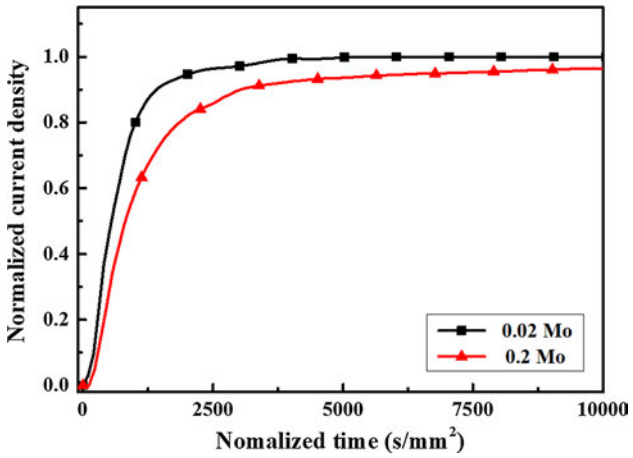

Fig. 9 Hydrogen permeation curves of 0.02 Mo and 0.2 Mo specimens

Table 4 Reversible H contents measured by TDS, hydrogen diffusion coefficient and concentration of reversible trap sites calculated by permeation test for the 0.02 Mo and 0.2 Mo specimens

	0.02 Mo	0.2 Mo
D_{eff} (m^2/s)	2.39×10^{-10}	1.49×10^{-10}
C_{rev} (mol/m^3)	0.45	0.77

decoration in 0.2 Mo steel [35, 36]. After saturating the specimen with hydrogen, hydrogen charging was interrupted, and the specimens were left for 5 min and 1 h, respectively, followed by reaction with an aqueous solution of $KAg(CN)_2$. In addition, microstructures trapping reversible hydrogen were observed with various periods of reversible hydrogen release after hydrogen charging. Fig. 10a shows the microstructure of the specimen left for 5 min, and the microstructures serving as reversible and irreversible trap sites were observed. The Ag particles were decorated near the MA constituents and grain boundaries. However, in the specimen left for 1 h (Fig. 10b), most of the hydrogen trapped at the reversible trap site was released outside, and Ag particles were observed in the grain, and not at the grain boundary or the MA constituents. Therefore, the MA constituents and grain boundaries were confirmed to be the reversible trap sites of hydrogen, which affected the diffusion behavior of reversible hydrogen.

Figure 11 shows the analysis of the MA constituents, in which reversible hydrogen was trapped in the 0.2 Mo steel specimen. Fig. 11a shows the specimen extracted from a section with Ag-decorated particles using FIB technique. The crystal structures of α' and γ in the FIB sample were observed by selected area diffraction pattern (SADP) (Fig. 11c and d), thereby identifying the existence of MA constituents (Fig. 11a). Furthermore, Fig. 11b shows Ag particles at the interface of MA constituents. Therefore, the interface between the MA constituents and matrix was confirmed to be a hydrogen trap site. Moreover, it is well-known that dislocation pile-up appears at the interface because hydrogen trapped in MA constituents reduces the repulsive force between dislocations [25]. Therefore, in this study, the increase in dislocation also increased the amount of hydrogen trapped around the interface, and the hydrogen and stress concentrations near the MA constituent promoted crack initiation.

The grain boundary also serve as a reversible trap site, and the 0.2 Mo steel showed a smaller grain size compared to that of the 0.02 Mo steel. Therefore, the effect of grain size on diffusion was compared based on the density of hydrogen traps (N_T) [37].

$$N_{T-GB}\left(\mathrm{cm}^{-3}\right) = \frac{30}{d_G\left(x_a\right)^2} \tag{4}$$

where d_G is the grain size, x_a is the atomic distance (0.26 nm), and the calculated $N_{T\text{-}GB}$ values are listed in Table 5. The $N_{T\text{-}GB}$ of 0.2 Mo steel was 1.5 times larger than that of 0.02 Mo steel, and 0.2 Mo steel had a more reversible hydrogen that could be trapped in the grain boundary. However, the degree of reduction in the grain size was insignificant, and Park et al. [38] also reported little variation in D_{eff} based on the grain size. Therefore, other factors were known to have a greater influence on the diffusion rate than the grain size.

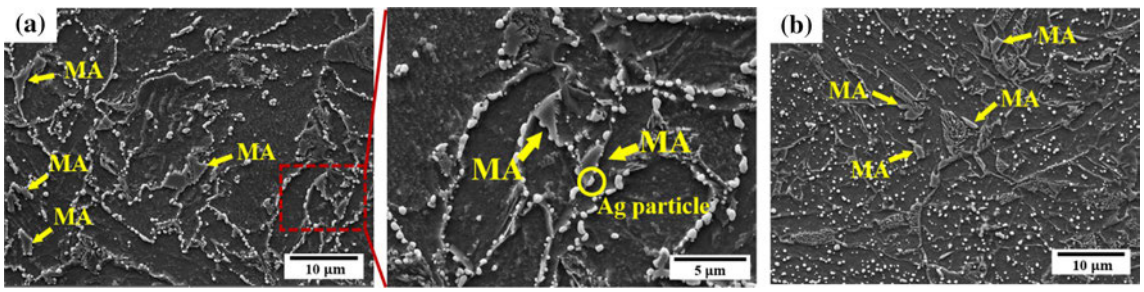

Fig. 10 SEM micrographs of silver decorated 0.2 Mo specimen maintained for various periods: **a** 5 min, **b** 1 h

Kim et al. [39] reported that the activation energy of hydrogen diffusion increased with an increase in the alloy elements such as, Cr, Mo, and Si in α-iron; indicating hydrogen was significantly trapped by generating a strain field owing to the dissolution of the alloy elements. In particular, Mo was effective for hydrogen trapping because of the large mismatch between the atomic radius and affinity with Fe atoms. The activation energy for the hydrogen diffusion of Mo solutes is known as 11.0 kJ/mol, which is similar to that of a reversible trap site such as grain boundaries and dislocations [6]. The density of the hydrogen trap (N_T) based on the Mo solute was obtained using Eq. 5 to confirm the effect of the Mo solute on the diffusion behavior [37] and is shown in Table 5.

$$N_{T-Mo}\left(cm^{-3}\right) = z\frac{mw_{Mo}}{M_{Mo}}N_A \quad (5)$$

where z is the six octahedral sites near the Mo atom, m is the mass of the experimental steel per volume ($m_{0.02Mo} = 7.55$ g/cm^3, $m_{0.2Mo} = 7.39$ g/cm^3), w_{Mo} is the weight concentration of Mo solute atom in the steel, and N_A is Avogadro constant. The $N_{T\text{-}Mo}$ of 0.2 Mo steel had a significantly higher $N_{T\text{-}Mo}$ compared to that of 0.02 Mo steel. The amount of reversible hydrogen measured with TDS and the reversible hydrogen trap density (C_{rev}) measured with the permeation test were high in 0.2 Mo steel with high $N_{T\text{-}Mo}$, and a decrease in the diffusion coefficient (D_{eff}) was also observed. In this study, a significant variation in $N_{T\text{-}Mo}$ was confirmed to be the major factor influencing the diffusion rate and HE resistance [6].

Despite the increase in MA constituents, the HE properties remained unchanged with an increase in Mo content to 0.2 wt%. This is because the apparent diffusion rate decreased owing to the increase in the number of reversible hydrogen trap sites, such as grain boundaries, MA constituents, and Mo solutes. The high hydrostatic stress near the sharp crack tip generated from MA constituents decreased the HE resistivity [40]; however, the reduction in the diffusion rate of reversible hydrogen by Mo solutes delayed the diffusion of reversible hydrogen in the region for 0.2 wt% Mo steel. Therefore, despite the change in crack initiation behavior owing to the HE-sensitive microstructure (MA constituents), a small change in the HE index was observed owing to the reduction in the diffusion rate of reversible hydrogen caused by Mo solutes. In other words, the 0.2 Mo steel was increased the strength while delaying the deterioration in HE resistance.

Table 5 Density of hydrogen trap by grain boundary and Mo solute

	0.02 Mo	0.2 Mo
$N_{T\text{-}GB}$ (cm^{-3})	2.61×10^{19}	4.03×10^{19}
$N_{T\text{-}Mo}$ (cm^{-3})	$9.47\times10^{18} - 5.68\times10^{19}$	$9.27\times10^{19} - 5.56\times10^{20}$

5 Conclusion

The present study investigated the effect of Mo on HE behavior in bainitic TMCP steels that increased the Mo content up to 0.2 wt% to attain high strength of off-shore steels. The important findings of this study are as follows.

(1) The increase in Mo content changed the microstructure from PF and DP to GB; in particular, the fraction of MA increased from 0.05 to 1.39%. In addition, the grain size decreased slightly with the addition of Mo (0.02 Mo steel and 0.2 Mo steel with grain sizes of 17 and 11 μm, respectively), and the precipitates showed no change in size or amount with (Ti, Nb)C and CuS observed in both specimens. The increase in Mo improved YS to ~ 13 MPa and TS to ~ 44 MPa, and both steels showed a decrease in elongation when hydrogen was charged. However, the difference in HE

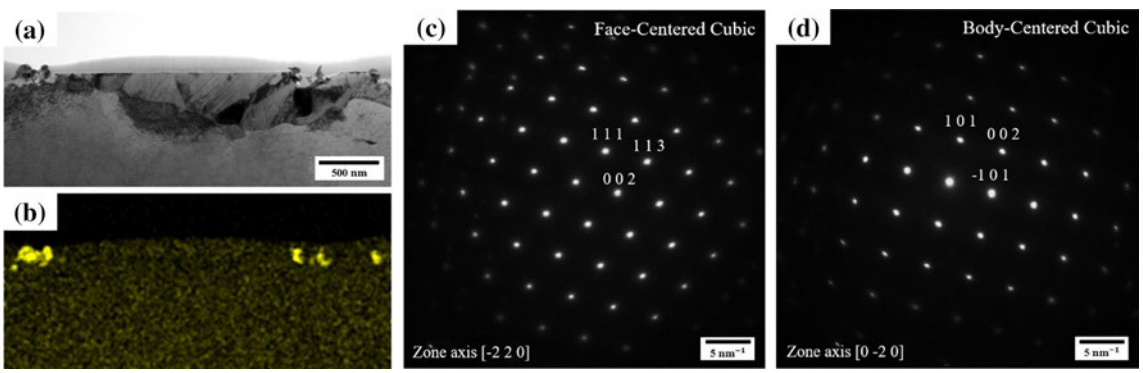

Fig. 11 FETEM micrographs of MA constituent post Ag decoration: **a** Bright field image, **b** EDS mapping of Ag element, **c** SADP of FCC, **d** SADP of BCC

index between the two steels was 3%; thus, there was little difference in HE resistance.

(2) For 0.02 Mo steel, the main crack initiation site was DP, and cracks/voids propagated in the same direction as the loading direction. For 0.2 Mo steel, the main crack initiation site was the MA constituents, and the propagation direction of the crack was sharply perpendicular to the loading direction. The MA constituents, which exhibited high strain in the KAM map after tensile testing, were sensitive to the initiation and propagation of cracks as hydrogen was charged.

(3) Despite the different HE cracking behaviors of the two steels, their HE resistance was almost the same. Through TDS analysis, a more reversible hydrogen desorption curve of 0.2 Mo steel was observed at ~ 110 °C compared to that of 0.02 Mo steel, and the measured reversible hydrogen content of 0.2 Mo steel was approximately three times higher. The diffusion of reversible hydrogen in 0.2 Mo steel was ~ 1.6 times slower than that of 0.02 Mo steel owing to the higher number of trap sites (MA constituents interface and Mo solutes) of the reversible hydrogen in 0.2 Mo steel. In particular, the trapping of hydrogen in the Mo solutes delayed the diffusion of reversible hydrogen into the crack tip of the MA constituents.

Acknowledgements This work was supported by the Technology Innovation Program–Materials and Components Development Program (Grant No. 20010453) funded by the Ministry of Trade, Industry, and Energy (MOTIE, Korea) and Fundamental Research Program (PNK-8750) of the Korea Institute of Materials Science (KIMS).

Author's contribution **JN**: Conceptualization, Investigation, Writing—original draft. **JL**: Data curation, Methodology. **HP**: Validation, Formal analysis. **CP**: Methodology, Visualization. **CL**: Resources, **JC**: Resources, Project administration. **S-GL**: Formal analysis, Visualization. **NK**: Conceptualization, Supervision, Writing—review & editing.

Data Availability Data will be made available on request.

Declarations

Conflict of interests The authors declare that they have no known competing financial interests or personal relationships that could have appeared to influence the work reported in this paper.

References

1. D.H. Shim, T. Lee, J. Lee, H.J. Lee, J.-Y. Yoo, C.S. Lee, Mater. Sci. Eng. A **700**, 473–480 (2017)
2. K. Junhua, Z. Lin, G. Bin, L. Pinghe, W. Aihua, X. Changsheng, Mater. Des. **25**, 723–728 (2004)
3. M.G. Kim, S.K. Cho, S.Y. Shin, J. Weld. Join. **40**, 22–32 (2022)
4. H. Lee, S.K. Cho, W.H. Choi, Y.G. Kim, Y.J. Kwon, J.G. Lee, S. Shin, D. Choi, J. Weld. Join. **39**, 269–277 (2021)
5. Y. Kang, C. Lee, J. Weld. Join. **39**, 233–238 (2021)
6. J. Yoo, M.C. Jo, M.C. Jo, S. Kim, S.-H. Kim, J. Oh, S.S. Sohn, S. Lee, Acta Mater. **207**, 116661 (2021)
7. C. Ledermueller, H.I. Pratiwi, R.F. Webster, M. Eizadjou, S.P. Ringer, S. Primig, Mater. Des. **185**, 108278 (2020)
8. H.-H. Jo, C. Shin, J. Moon, J.H. Jang, H.-Y. Ha, S.-J. Park, T.-H. Lee, B.H. Lee, J.-H. Chung, J.G. Speer, Mater. Des. **194**, 108882 (2020)
9. D. Zhang, W. Li, X. Gao, L. Fu, J. Guo, J. Zhang, Q. Pang, Z. Xu, Mater. Sci. Eng. A **845**, 143220 (2022)
10. S. Zhang, Y. Huang, B. Sun, Q. Liao, H. Lu, B. Jian, H. Mohrbacher, W. Zhang, A. Guo, Y. Zhang, Mater. Sci. Eng. A **626**, 136–143 (2015)
11. H.-J. Kim, S.-H. Jeon, W.-S. Yang, B.-G. Yoo, Y.-D. Chung, H.-Y. Ha, H.-Y. Chung, J. Alloys Compd. **735**, 2067–2080 (2018)
12. G.T. Park, S.U. Koh, K.Y. Kim, H.G. Jung, Corros. Sci. Tech. **5**, 117–122 (2006)
13. G.T. Park, S.U. Koh, H.G. Jung, K.Y. Kim, Corros. Sci. **50**, 1865–1871 (2008)
14. H. Park, C. Park, J. Lee, N. Kang, S. Liu, Corros. Sci. **181**, 109229 (2021)
15. D.C. Ramachandran, J. Moon, C.-H. Lee, S.-D. Kim, J.-H. Chung, E. Biro, Y.-D. Park, Mater. Sci. Eng. A **801**, 140390 (2021)
16. I. Kim, M. Lee, Y. Choi, N. Kang, Steel Res. Int. **89**, 1700278 (2018)
17. S.-W. Lee, S.-I. Lee, B. Hwang, Korean J. Mater. Res. **27**, 524–529 (2017)
18. Y. Luo, H. Lu, N. Min, W. Li, X. Jin, Mater. Sci. Eng. A **844**, 143108 (2022)
19. I. Moro, L. Briottet, P. Lemoine, E. Andrieu, C. Blanc, G. Odemer, Mater. Sci. Eng. A **527**, 7252–7260 (2010)
20. S.K. Dwivedi, M. Vishwakarma, Int. J. Hydrogen Energ. **43**, 21603–21616 (2018)
21. J. Lee, H. Park, M. Kim, H.-J. Kim, J. Suh, N. Kang, Met. Mater. Int. **27**, 166–174 (2021)
22. G.M. Ugiansky, J.H. Payer (eds.), Stress Corrosion Cracking: The Slow Strain-Rate Technique ASTM International, West Conshohocken, **665** (1979)
23. C. Park, N. Kang, S. Liu, J. Lee, E. Chun, S.-J. Yoo, Met. Mater. Int. **25**, 584–593 (2019)
24. H. Park, C. Park, J. Lee, H. Nam, B. Moon, Y. Moon, N. Kang, Mater. Sci. Eng. A **820**, 141568 (2021)
25. E.V. Chatzidouros, V.J. Papazoglou, D.I. Pantelis, Int. J. Hydrogen Energ. **39**, 18498–18505 (2014)
26. A.I. Hwang, D.G. Lee, Y. Jung, J.-M. Koo, J.D. Cho, J.S. Lee, D.-W. Suh, Met. Mater. Int. **27**, 3959–3967 (2021)
27. H. Addach, P. Berçot, M. Rezrazi, J. Takadoum, Corros. Sci. **51**, 263–267 (2009)
28. S. Frappart, X. Feaugas, J. Creus, F. Thebault, L. Delattre, H. Marchebois, J. Phys. Chem. Solids **71**, 1467–1479 (2010)
29. L. Lan, X. Kong, Z. Hu, C. Qiu, D. Zhao, L. Du, Corros. Sci. **112**, 180–193 (2016)
30. J. Lee, C. Park, H. Park, N. Kang, Int. J. Hydrogen Energ. **45**, 10227–10232 (2020)
31. C. Park, N. Kang, M. Kim, S. Liu, Mater. Lett. **235**, 193–196 (2019)
32. ISO 17081, Method of measurement of hydrogen permeation and determination of hydrogen uptake and transport in metals by an electrochemical technique (IOS, Geneva,2014)
33. J.H. Park, M. Oh, S.J. Kim, J. Mater. Res. **32**, 1295–1303 (2017)
34. K.-M. Ryu, D.G. Lee, J. Moon, C.-H. Lee, T.-H. Lee, J.S. Lee, D.-W. Suh, Met. Mater. Int. **27**, 425–435 (2021)
35. H. An, J. Lee, H. Park, J. Yoo, S. Chung, J. Park, N. Kang, Korean J. Met. Mater. **59**, 21–32 (2021)
36. H. Park, B. Moon, Y. Moon, N. Kang, Metals **11**, 1039 (2021)
37. Y. Liu, M. Wang, G. Liu, Int. J. Hydrogen Energ. **38**, 14364–14368 (2013)

38. C. Park, N. Kang, S. Liu, Corros. Sci. **128**, 33–41 (2017)
39. K.T. Kim, J.K. Park, J.Y. Lee, S.H. Hwang, J. Mater. Sci. **16**, 2590–2596 (1981)
40. X. Li, X. Ma, J. Zhang, E. Akiyama, Y. Wang, X. Song, Acta Metall. Sin. Engl. Lett. **33**, 759–773 (2020)